S9

STRUCTURAL AND MORPHOLOGICAL PROPERTIES OF Fe_2O_3/TiO_2 NANOCRYSTALS IN SILICA MATRIX

Václav Valeš[1], Václav Holý[1], Maja Buljan[2], Vesna Janicki[2], and Sigrid Bernstorff[3]

[1]*Department of Condensed Matter Physics, Charles University in Prague, Czech Republic*
[2] *Rudjer Boskovic Institute, Zagreb, Croatia*
[3] *ELETTRA Sincrotrone Trieste, Basovizza, Italy*

Titania (TiO_2)-based systems have been very intensively studied in last decades because of their photocatalytic activity, which found broad commercial applications. Functionalized titania composites, especially Fe_2O_3/TiO_2 systems attracted a lot of attention recently (see [1, 2], among others), since they make it possible to improve the photocatalytic performance of titania. The -phase of Fe_2O_3 exhibits a very large magnetic coercivity at room temperature [3] so that Fe_2O_3/TiO_2 in solutions can easily be manipulated by external magnetic field. Fe_2O_3/TiO_2 compact thin layer composites as a photocatalyst can respond to visible light due to the narrow band-gap of Fe_2O_3.

We have studied two types of structures, namely $(Fe_2O_3+SiO_2)/SiO_2$ and $(Fe_2O_3+SiO_2)/(TiO_2+SiO_2)/SiO_2$ periodic multilayers. Both types of samples were grown by a co-deposition of the actual material together with SiO_2 and pure SiO_2 as an interlayer spacer. The samples have been subsequently annealed for one hour at various temperatures in air or forming gas (FG – Ar + 4% H_2). We prepared a large series of samples with various thicknesses, annealing temperatures and annealing atmospheres in order to find the optimal conditions of the preparation; here we report only several characteristic examples, their basic parameters are summarized in Tab. 1. Samples A – F consist of 10 periods, samples A – C were annealed in forming gas atmosphere, while samples D – F at the air. Samples that did not contain titania were prepared under various conditions – thickness of $Fe_2O_3 + SiO_2$ layer from 0.6 nm to 2.0 nm, annealing temperature from 300 °C to 900 °C at air, forming gas, or vacuum. These samples consisted of 20 periods.

X-ray diffraction curves of the samples have been measured by laboratory diffractometer with a standard x-ray tube (CuK radiation, 1.5 kW) using a parallel-beam setup. During the measurement the angle of incidence of the primary beam was kept constant at 1 deg to suppress the substrate signal.

Small-angle X-ray scattering in grazing incidence geometry (GISAXS method) has been carried out at ELETTRA synchrotron source (SAXS beamline) using the photon energy of 8 keV. The incidence angle of the x-ray beam was chosen 0.25 deg, i.e. just above the critical angle of total external reflection.

The X-ray diffraction data on samples without titania exhibit diffraction maxima neither before, nor after post-growth annealing, i.e., the Fe_2O_3 component did not crystallize under the annealing conditions used in this work. The diffraction curves of samples A-F are presented in Figure 1. From the data it follows that TiO_2 nanoparticles grow during the annealing, from the positions of their diffraction peaks we identified the tetragonal rutile phase. More interestingly, in samples E and F we detected also

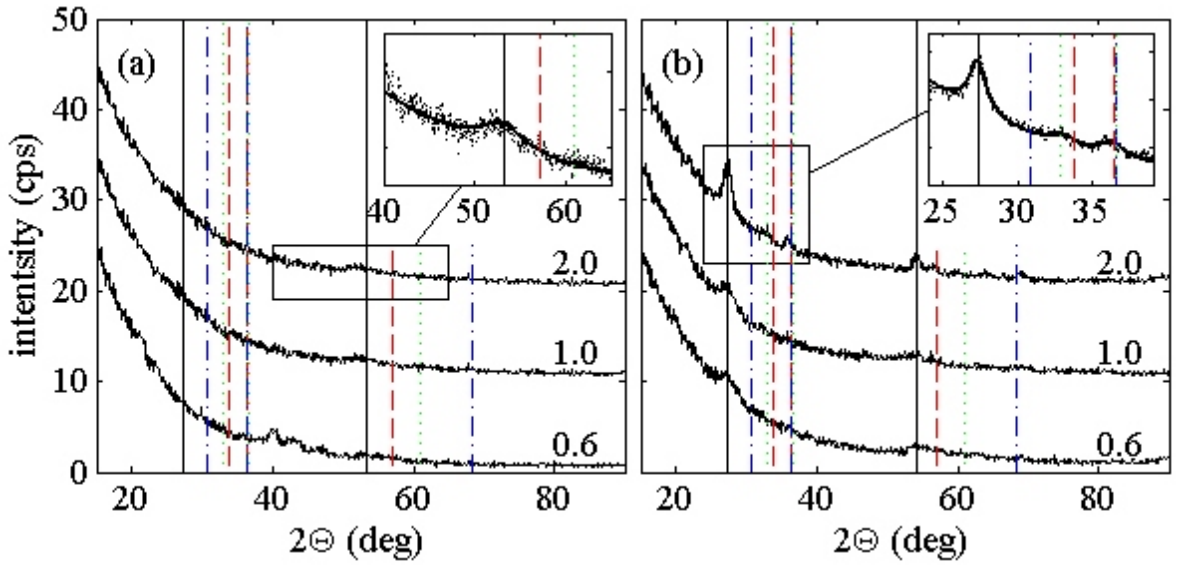

Figure 1. X-ray diffraction curves of samples A, B, C (a) and D, E, F (b). The insets display the details of the diffraction peaks along with their fits to theoretical curves (lines). The vertical lines indicate the theoretical positions of the diffraction peaks for various phases: black full line – rutile, red dashed line – hematite (-Fe_2O_3), blue dash-dotted line – maghemite (-Fe_2O_3), and green dotted - -Fe_2O_3.

Table 1. Parameters of the TiO_2-containing multilayers determined from X-ray diffraction and GISAXS methods, all values are in nm. d is the nominal thickness of layers, T is the annealing temperature, R_L, R_V are lateral and vertical diameters of particles resp., a_L, a_V are mean base lateral and vertical vectors and $_L$, $_V$ are their rms.

Sample	d	T (°C)	x-ray diffraction	GISAXS							
			R_{TiO2}	R_{Fe2O3}	R_L	R_V	a_L	a_V	$_L$	$_V$
A	0.6	700			1.8 1.0	1.8 1.0	3 3	10.0 0.5	2 1	5 1
B	1.0	700			2.5 1.0	1.5 1.0	3 3	11.5 0.5	2 1	4 1
C	2.0	700			3.5 1.0	1.5 1.0	8 3	12.5 0.5	2 1	4 1
D	0.6	900	1.6 1.0							
E	1.0	900	2.1 1.0		3.0 0.5	2.0 0.5	16 5	10.0 0.5	5 1	5 1
F	2.0	900	3.2 1.0	2.7 1.0	5.0 0.5	3.0 0.5	16 5	11.5 0.5	5 1	10 1

Fe_2O_3 nanoparticles, however their diffraction maxima are rather weak, which indicates that the density of these particles is very small. The positions of the Fe_2O_3 maxima roughly correspond to the hexagonal hematite -Fe_2O_3 or -Fe_2O_3 phase. We have compared the diffraction maxima with the simulations based on the Debye-formula approach [2] assuming spherical particles and from this comparison we estimated the mean particles sizes (Tab. 1).

From the fitting of experimental GISAXS data we found that the (Fe_2O_3+SiO_2)/SiO_2 multilayers exhibit no diffraction peaks and no side maxima in GISAXS intensity maps. Therefore, they remain amorphous and do not form any ordered structure of amorphous or crystalline particles during post-growth annealing at temperatures up to 900°C. On the other hand, the multilayers (Fe_2O_3 + SiO_2)/ (TiO_2 + SiO_2)/SiO_2 exhibit both diffraction peaks and GISAXS side maxima after annealing, thus they contain ordered array of crystalline particles. In these samples, both rutile TiO_2 and hematite -Fe_2O_3 are present, the latter with much smaller occurrence. Therefore, the presence of the TiO_2 phase facilitates the crystallization of Fe_2O_3 during post-growth annealing. Increasing the thicknesses d of the Fe_2O_3 and TiO_2 layers, the mean lateral size of the particles increases; the vertical size however remains almost constant so that the particles are disc-shaped for larger d. A similar trend of increasing the lateral particle size is observed for increasing annealing temperature. The number of the observed diffraction peaks did not make it possible to determine the lateral and vertical sizes. The particle size determined from diffraction is affected by possible deformation of the particle lattice and/or by structural defects, therefore a detailed comparison of the particle sizes determined from both methods is not possible. Nevertheless, the particle sizes obtained from x-ray diffraction and GISAXS data are not in contradiction.

1. H. Cui, W. Ren, W. Wang, J. Sol-Gel Sci. Technol. **58**, 476 (2011).
2. V. Valeš, J. Poltierová Vejpravová, V. Holý, V. Tyrpekl, P. Brázda, and S. Doyle, phys. stat. solidi C **7**, 1399 (2010).
3. J. Jin, K. Hashimoto, and S. Ohkoshi, J. Magn. Magn. Mater. 15, 1067 (2005).

The work was supported by the Czech Science Foundation (project P204-11-0785) and by the Grant Agency of Charles University in Prague (project SVV 263307).

S10

STRUCTURAL STUDY OF TITANATE NANOTUBES

T. Brunátová[1], D. Králová[1], S. Daniš[1], M. Šlouf[2], R. Kužel[1]

[1]*Charles Univ., Faculty of Mathematics and Physics, Dep. of Condensed Matter Physics, Prague, Czech Rep*
[2]*Inst. of Macromolecular Chemistry, Academy of Sciences of the Czech Republic, Prague, Czech Republic*

TiO_2 based materials achieved broad applications. Titanate nanotubes (Ti-NT) have big surface area which is also suitable for catalytic application. Another potential application of Ti-NT is using them in lithium batteries to improve the rate of diffusion of intercalated lithium ions – small size of lithium ions and structure of Ti-NT – ionic transport in interlayer [1]. But the structure of Ti-NT is not clearly understood and different possible structures are reported. The first was the anatase structure identified by Kasuga et al. [2]. Then indications of sodium ions in the structure of Ti-NT appeared [e.g. 3, possible structure $Na_2Ti_2O_4(OH)_2$ or $H_2Ti_2O_4(OH)_2$]. Other structures reported were trititanate [4] ($H_3Ti_2O_7$) or sodium trititanate ($Na_3Ti_2O_7$), $H_2Ti_2O_5$ H_2O [5] or for example $H_2Ti_4O_9$ H_2O [6]. In [5], the study of dependence of Ti-NT structure on time of hydrothermal method, it was shown how the nanotubes were created – by rolling the 2D sheet.

The samples investigated were prepared at the Institute of Macromolecular Chemistry, Academy of Sciences of the Czech Republic, Prague, Czech Republic. The preparation method was a simple hydrothermal treatment of initial powder. In this work, microcrystalline rutile was used as a starting TiO_2 powder. Hydrothermal method consists in boiling the initial TiO_2 powder with 10M NaOH. Then obtained powder was neutralized by HCl and dried. More about preparation can be found in [7].

The samples were measured in the transmission geometry in diffractometer Rigaku Rapid II with Mo-K radiation, 0.3 mm collimator and 2D image plate detector. Ti-NT were measured in copper wire holder formed into a loop. Measured X-ray 2D pattern was converted into conventional powder X-ray pattern by the software 2DP.

Possible Ti-NT was identified as a beta phase of TiO_2 [8]. Comparison of measured powder X-ray diffraction (PXRD) pattern and theoretical position of peaks of -TiO_2 (monoclinic, a = 12.1787 Å, b = 3.7412 Å, c = 6.5249 Å, = 107.054° [9]) can be seen on Figure 1. Nanotube was made by rolling 2D sheet made from this structure. The variable parameters in the model were the lattice parameters and multiplicity of all the parameters except . The multiplicity of c is given by the number of walls in a nanotube. This multiplicity could be estimated from the electron microscopy. The multiplicity of other parameters a,b have effect only on the width of diffraction peaks. The sharp peak at 2 ~ 22° corresponds to the tube length – the tube axis is given by the parameter b and consequently its value can be determined directly. For estimation of other parameters computer simultaneous by using the Debye formula were performed.

Final simulated patterns were convoluted with the Gauss function describing the instrumental function of the diffractometer. The best agreement of calculated and experimental data achieved so far can be seen on Fig. 2.

1. Bavykin D.V., Walsh F.C.:Elongated Titanate nanostructures and Their Applications, European Journal of Inorganic Chemistry, 2009.
2. Kasuga T., Hiramatsu M., Hoson A., Sekino T., Niihara K.: Formation of Titanium Oxide Nanotube, Langmuir, 14, 1998.
3. Yang J., Jin Z., Wang X., Li W., Zhang J., Zhang S., Guo X., Zhang Z.: Study on composition, structure and formation process of nanotube $Na_2Ti_2O_4(OH)_2$, Dalton, 2003.
4. Chen Q., Zhou W., Du G., Peng L.-M.: Trititanate nanotubes made via a single alkali treatment, Advanced materials, 14, 2002.
5. Chen W., Gou X., Zhang S., Jin Z.: TEM study on the formation mechanism of sodium titante nanotubes, Journa of Nanoparticle Research, 9, 2007.

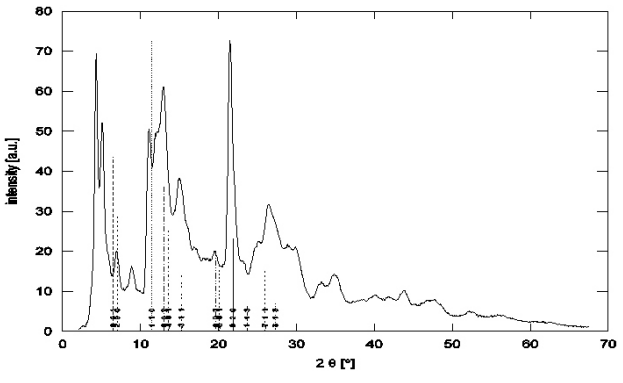

Figure 1. Measured PXRD pattern and theoretical positions of peaks of structure beta TiO_2

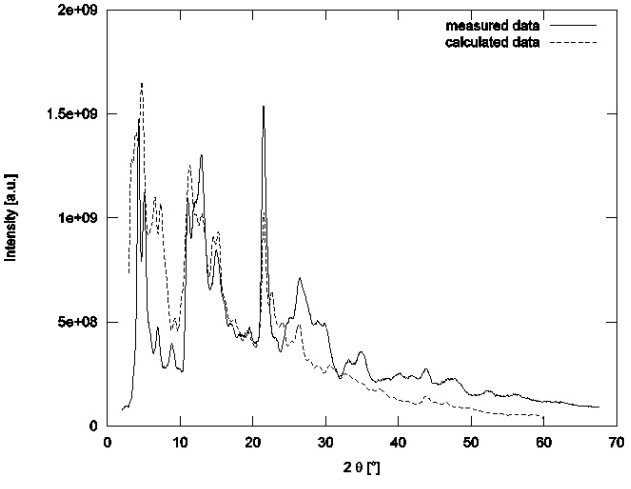

Figure 2. Comparison of measured and calculated PXRD pattern.

6. Nakahira A.,Kato W., Tamai M., Isshiki T., Nishio K.: Synthesis of nanotube from a layered $H_2Ti_4O_9$ H_2O in a hydrothermal treatment using various titania sources, Journal of materials science, 39, 2004.
7. Králová D., Pavlova E.,Šlouf M., Kužel R.: Preparation and structure of titanate nanotubes, Materials Structure, vol. 15, 2008.
8. T.Brunatova, D. Králová, M. Šlouf, S. Daniš, R Kužel: X-ray study of structure of TiO2 nanotubes and nanowires, Zeitschrift fuer Kristallographie, in press.
9. ICDD database PDF-4, card number 74-1940.

Extended contribution submitted.

S11

STUDY OF ZIRCONIUM BASE ALLOYS BY NEUTRON DIIFRACTION

M. Krůželová, S. Vratislav, M. Dlouhá

Department of Solid State Engineering, FNSPE, CTU, Trojanova 13, 120 00, Prague 2, Czech Republic
monika.kruzelova@fjfi.cvut.cz

Neutron diffraction is a very powerful tool in texture analysis of zirconium base alloys used in nuclear technique [1]. Textures of five samples (two rolled sheets and three tubes) were investigated by using direct pole figures, inversion pole figures.

The texture measurements were performed at diffractometer KSN2 at Laboratory of Neutron Diffraction, Department of Solid State Engineering, Faculty of Nuclear Sciences and Physical Engineering, CTU in Prague. The wavelength used was = 0.1362 nm. The data were processed using software packages HEXAL [2] and GSAS [3].

Basal pole figures

Basal pole figures were measured for samples Zr1, Zry2, and ZiT [4] (Fig. 1).

Inverse pole figures

Inverse pole figures were calculated for samples Zrp, Zry2, ZiT, and ZrW. The intensity ratios were calculated by Mueller formula [5]. Calculated inverse pole figures are at Tab. 1 [4]. The intensity ratios are relative to the non-texture stage.

Discussion and Conclusions

Our results can be summarized as follows:

All samples of zirconium alloys show the distribution of middle area into two maxims in all basal pole figures. This is caused by alloying elements. A characteristic split of the basal pole maxima tilted from the normal direction toward the transverse direction can be observed for all samples.

- Sheet samples prefer orientation of planes (100) and (110) perpendicular to rolling direction and orientation of planes (002) perpendicular to normal direction.
- Basal planes of tubes are oriented parallel to tube axis; meanwhile (100) planes are oriented perpendicular to tube axis.
- Level of resulting texture and maxima position is different for tubes and for sheets.

Zirconia-based alloys are used in nuclear technology, and our results are consistent with data published by other authors [6].

1. G. E. Bacon, *Neutron Diffraction*, 3rd ed., Oxford: Clarendon Press, 1975.

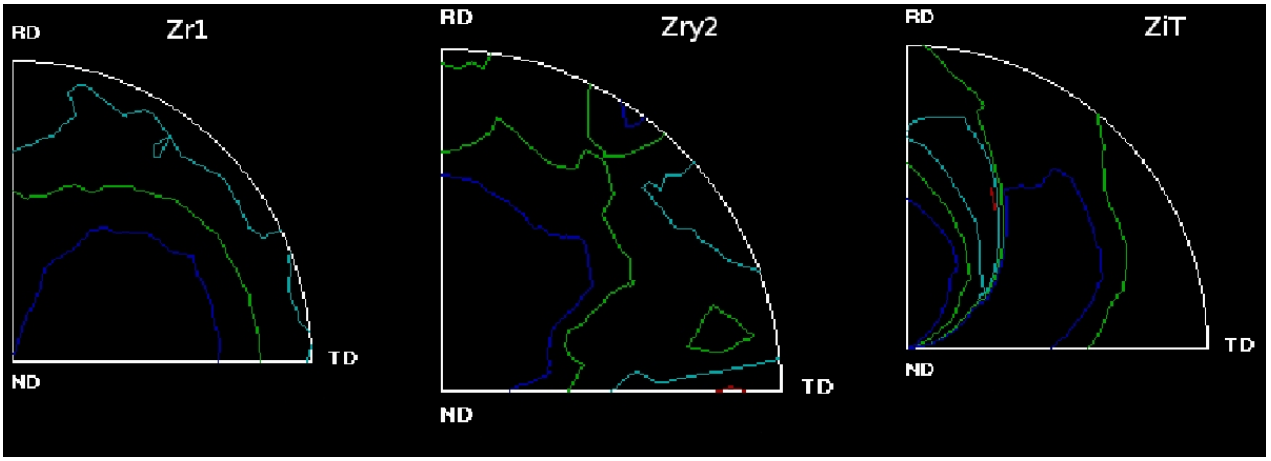

Figure 1. Comparison of basal pole figures of zirconium samples Zr1, Zry2, and Zit. System of coordinates is represented by ND, RD, and TD.

Table 1. Calculated inverse pole figures of samples Zrp, Zry2, ZrW, and ZiT.

Sample	p002, ND	p002, (0,45)	p100, RD	p100, TD	p110, RD
Zrp	3.076	N	2.742	1.173	1.678
Zry2	1.702	1.729	1.173	0.886	2.780
ZiT	1.158	1.807	3.767	0.747	0.719
ZrW	1.170	2.403	2.951	0.444	0.788

2. M. Dlouhá, L. Kalvoda, S. Vratislav, B. Cech, *Texturní analýza trubek ze zirkoniových slitin neutronovou difrakcí*, Kovové materiály 4.29, Bratislava, 1991.
3. A.C. Larson, R.B. Von Dreele, *General Structure Analysis System (GSAS)*, Los Alamos National Laboratory Report LAUR 86-748, 1994.
4. M. Kruželová, *Studium vlastností slitin na bázi zirconia metodou neutronové difrakce*, Diplomová práce, ceské vysoké ucení technické v Praze, Fakulta jaderná a fyzikálne inženýrská, Katedra inženýrství pevných látek, 2010.
5. R. M. S. B. Horta, W. T. Roberts, D. V. Wilson, *Texture representation by inverse pole figures*, Technical report, TMS - AIME, 1969.
6. A. V. Nikulina, *Zirconium Alloys in Nuclear Power Engineering*, Metal Science and Heat Treatment, 46, 2004, pp. 458 - 462.

Extended contribution submitted.

S12

INVESTIGATIONS OF REAL STRUCTURE DEPTH DISTRIBUTIONS IN METALS USING DIFFRACTION TECHNIQUES

Z. Pala

Department of Solid State Engineering, Faculty of Nuclear Sciences and Physical Engineering, Czech Technical University in Prague, Trojanova 13, 120 00 Prague 2, Czech Republic
zdenek.pala@fjfi.cvut.cz

In the case of metals, X-ray diffraction (XRD) is often regarded as a surface technique which reveals structural information about diffracting body only several micrometers or tens of micrometers in thickness. Yet in comparison with electron diffraction, assumption about surface sensitivity would be hardly tenable. On the other end of the penetration scale, neutron diffraction is firmly anchored because the neutrons penetrate metallic materials more easily and the resulting data can be gained from depths amounting to centimetres.

Notion of penetration depth, which was initially introduced by Cullity [1], is of vital importance from the real structure point of view. The main reason is that metal objects, especially those with surface treatment history, often show significant depth gradients of macroscopic and microscopic residual stress, grain sizes, or even texture. Gradients of these real structure characteristics have direct impact on the object behaviour in real environment, affecting its corrosion resistance, dynamic load stability, crack initiation and propagation and other processes that can contribute to either prolongation or appreciable shortening of fatigue life [2].

The effective penetration depth is given by (i) absorption μ of the given volume for the impinging X-ray beam wavelength, (ii) Bragg angle and (iii) geometric alignment of the goniometer f(. Applying the well known Lambert-Beer law for absorption, the ratio of intensities diffracted by a layer of thickness dT on the very surface and in the depth T will be

$$\frac{dI_T}{dI_{T\ 0}} \quad \exp(\quad Tf(\ , \ )), \tag{1}$$

Upon setting this ratio to a convenient constant of 1/e and taking a logarithm of the (1), the term for effective penetration depth T^e is calculated:

$$T^e \quad \frac{1}{f(\ , \ )}. \tag{2}$$

Hence, T^e determines the thickness of a layer providing 63.2 % out of the entire diffracted intensity. Rigorously said, the structural information gained from classical Bragg-Brentano goniometer or even grazing incidence diffraction changes with the changing 2 angle and is, therefore, influenced by possible steep structural gradients. However, when the gradients are not to be expected within the comparatively small thickness comparable with T^e, the depth profiling can be performed with combining the chosen XRD technique on a conventional laboratory diffractometers and subsequent layer removal. Inherently destructive layer removal should be done with minimal im-

pact to the structure of the remaining layers; the most widely used technique is electro-chemical polishing [3]. Even the laboratory diffractometers offer possibility to change X-ray tube and, accordingly, the used wavelength. This would allow corresponding alteration of T^e, yet given the variety of X-ray tube selection, the scope of T^e for given metal is quite limited.

Another possibility for depth distribution investigation in metals is to employ synchrotron radiation. Not only is it tuneable with maximal energies peaking at 150 keV, but the intensities increase manyfold. The experimental set-up of *1ID C* beamline at APS (Advanced Photon Source) in Argonne, USA depicted in Fig. 1 is almost an ideal tool for defined depth profiling. The incoming X-ray beam can be focused down to 2 × 5 m and with maximal energy of 130 keV can easily penetrate 1 cm of steel, with large detector array High Energy Detector Array or HYDRA© the minimal acceptable transmission reaches 0.1 %.

The presentation will deal with detailed description of advantages and pitfalls of diffraction experiment at *1 ID C*. Furthermore, a mutual comparison between conventional XRD laboratory and synchrotron experiment results will be offered. Tangibly, macroscopic residual stress profiles in ground steel will be compared. Moreover, depth distributions of structure in plasma sprayed tungsten and copper layers used as plasma facing components in tokamaks obtained with use of neutron diffraction [4]and synchrotron radiation will be discussed.

Possibility to measure and study depth distributions of real structures parameters represent a further step in the progress of diffraction techniques and bring them nearer to the wider public. In this case, the industrial applications are, indeed, numerous and significantly broaden horizons of material scientists and physical engineers during new material evolution and manufacturing of metal objects used in hi-tech applications.

1. B.D. Cullity, *Elements of X-ray diffraction.* Reading: Addison -Wesley. 1956.
2. A. G. Youtsos, *Residual stress and its effect on fracture and fatigue*. Springer 2006.
3. S. Lee, Y. Lee, M. Chung, *Metal removal rate of the electrochemical mechanical polishing technology for stainless steel – the electrochemical characteristics*, IMechE Vol. 220, 2006.
4. V. Luzin, J. Matejicek, T. Gnaupel-Herold, *Through-thickness Residual Stress Measurement by Neutron Diffraction in Cu+W Plasma Spray Coatings*, Materials Science Forum 652 (2010) 50-56.

The research was supported by the Project MSM 6840770021 of the Ministry of Education, Youth and Sports of the Czech Republic and by the Project SGS10/300/OHK4/3T/14 of the Czech Technical University in Prague.

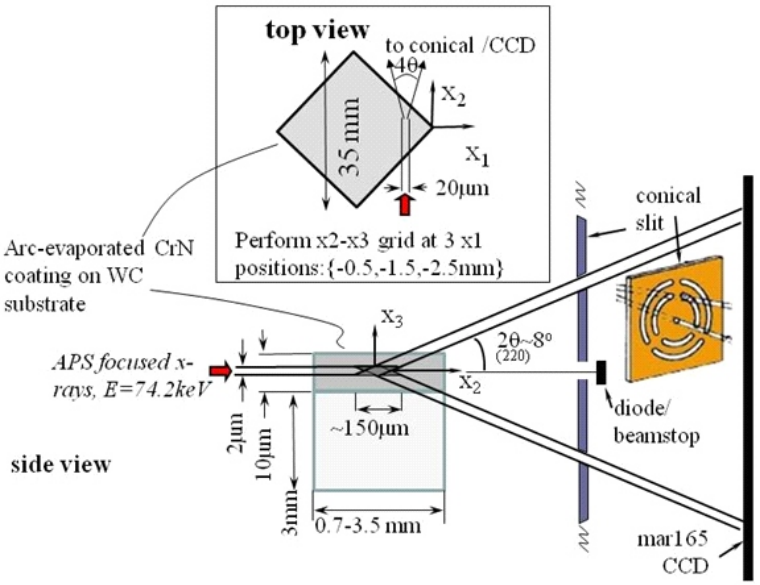

Figure 1. Experimental set-up of *1 ID C* in APS, Argonne; courtesy of Jonathan Almer.

S13

FÁZOVÁ TRANSFORMACE V AUSTENITICKÉ OCELI VYVOLANÁ PLASTICKOU DEFORMACÍ

J. Drahokoupil[1] , P. Haušild [1], V. Davydov [2] and P. Pilvin[3]

[1]FJFI ČVUT, Trojanova 13, 120 00 Praha 2, ČR
[2]UJF AV ČR , v.v.i. , 250 68 Řež, ČR
[3]Laboratoire d'Ingénierie des Matériaux de Bretagne, Université de Bretagne-Sud, Rue de Saint Maudé, BP 92116, 56321 Lorient, France
draho@fzu.cz

Úvod

V austenitické oceli s nízkým obsahem niklu dochází vlivem formování za studena k fázové transformaci z kubického plošně centrovaného -austenitu na kubický prostorově centrovaný ´-martenzit a na hexagonální -martenzit [1]. Cílem tohoto výzkumu bylo porovnat charakterizaci martenzitické transformace v metastabilní austenitické oceli pomocí tří difrakčních technik (rtg, neutrony, EBSD). Kromě fázové transformace byla pozorována i textura a v případě rtg difrakce také vývoj velikosti krystalitů na vložené deformaci.

Materiál a experiment

Jako vzorky byly použity plechy tlouš•ky 0,68 mm z chrom-niklové austenitické oceli od firmy Arcelor-Mittal odpovídající označení AISI 301. Vzorky byly nataženy o 5%, 10%, 15% a 20% na přístroji INSPEKT 100kN a poté pozorovány ve světleném mikroskopu Neophot 32. EBSD byla provedeno na zařízení SEM FEI Quanta 200 FEG s EBSD analyzátorem TSL™. Pro rentgenová difrakční měření byl použit difraktometr X´Pert PRO s texturním nástavcem ATC-3, Co lampou a detektorem X´Celerator. Neutronová difrakce byla provedena na diffraktometru TEXTDIFF na reaktoru LVR-15 v Řeži.

Výsledky a diskuse

Světelná mikroskopie. Mikrostruktura počátečního stavu a po různém stupni plastické deformace je zobrazena na obr. 1.

V nedeformovaném stavu je struktura tvořena velkými austenitickými zrny z typickou dvojčatovou strukturou. Vlivem plastické deformace se v těchto zrnech začínají objevovat martenzitické oblasti. Množství martenzitu se s rostoucí plastickou deformací zvětšuje až fáze martenzitu začne převládat na původním austenitem.

Fázová analýza. Všechny tři difrakční techniky prokázali, že deformační proces transformuje původní austenit převážně na ’-martenzit. V zanedbatelném množství byl pozorován i -martenzit. Procentuální objemové zastoupení plasticky indukovaného martenzitu je pro všechny tři difrakční techniky ve shodě s kinetickou rovnicí [2]. Objem martenzity se zvětšuje s rostoucí deformací, až postupně převáží nad původním austenitem dosahujíc hodnoty okolo 70%, viz obr. 2.

Textura. Původní válcovací textura se během deformačního procesu téměř nezměnila, což opět potvrdili všechny tři difrakční techniky. Pólové obrazce pro nedeformovaný vzorek a vzorek po 20% deformaci se téměř neliší. Během fázové transformace se roviny původní roviny {111} austenitu mění na roviny {110} ’-martenzitu, viz obr. 3.

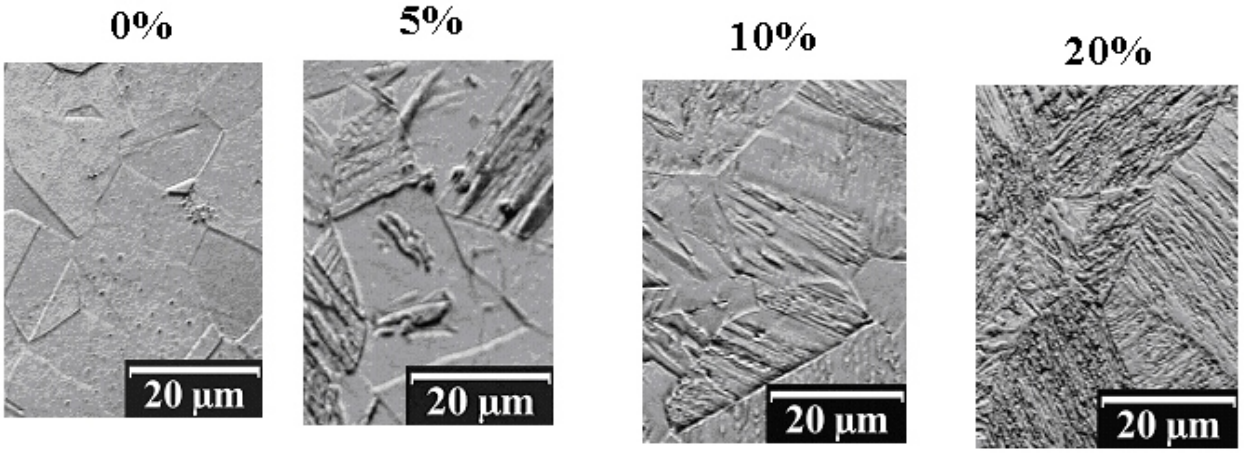

Obrázek 1. Mikrostruktura oceli AISI301 v nedeformovaném stavu a po několika úrovních plastické deformace.

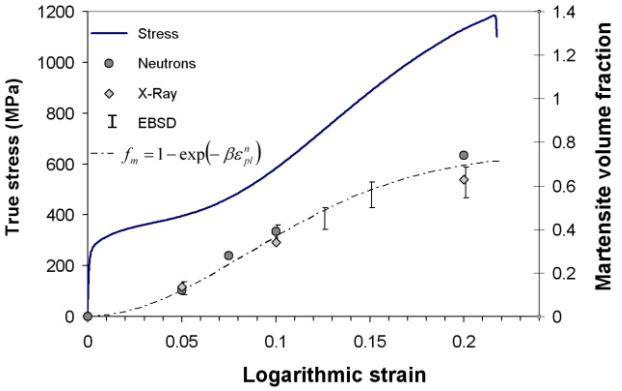

Obrázek 2. Vývoj objemové frakce ' martenzitu po plastické deformaci.

Velikost krystalitů. Stanovení velikosti krystalitů bylo komplikováno texturou, která omezuje množství pozorovatelných difrakcí pro danou orientaci vzorku, elastickou anizotropií, která komplikuje separaci deformační a velikostního rozšíření a pravděpodobnou směrovou závislostí velikostí krystalitů způsobenou orientováno deformací. Proto byla vybrána tato dvojice difrakcí {111}-{222} pro austenit a {110}-{220} pro martenzit a vzorek natočen o cca 25° od normály povrchu. Byla provedena korekce na rozšíření způsobeného nakloněním vzorku. Závislost velikosti částic na stupni deformace je ukázána na obr. 4.

1. L. Mangonon Jr., G. Thomas: Metall. Trans. **1** (1970), p. 1577.

2. H.C. Shin, T.K. Ha, Y.W. Chang: Scripta Mater. **45** (2001), p.823

Tato práce vznikla za finanční podpory Grantové agentury České republiky zkrze grant č. 101/09/0702 a také díky projektu studentské grantové soutěže ČVUT č. SGS 10/300/OHK4/3T/14.

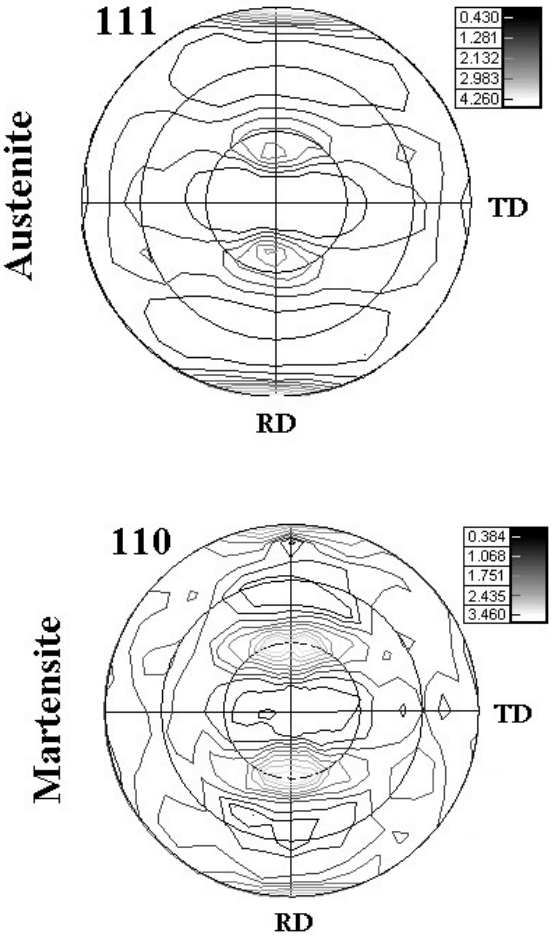

Obrázek 3. RTG pólové obrazce rovin {111} austenitu a {110} martenzitu pro vzorek s 10% deformací.

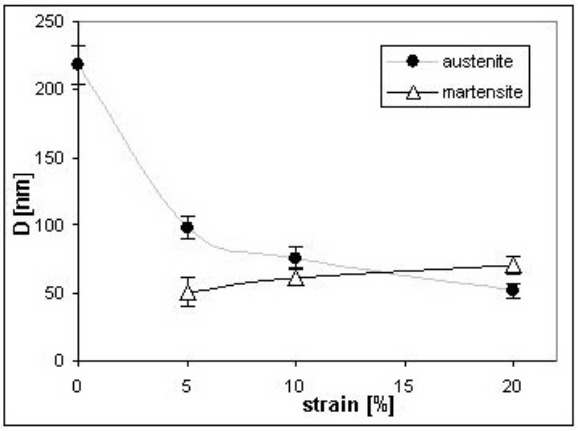

Obrázek 4. Vývoj velikosti krystalitů s úrovní deformace.